Numerical Simulation of a Near-Wall Bubble Collapse in an Ultrasonic Field*

Aljaž OSTERMAN**, Matevž DULAR** and Brane ŠIROK**

** University of Ljubljana, Faculty of Mechanical Engineering
Askerceva 6, SI-1000 Ljubljana, Slovenia
E-mail: aljaz.osterman@fs.uni-lj.si

Abstract

Ultrasonic cleaning device was modeled and the collapse of a single bubble in an ultrasonic pressure field was studied using a finite-volume 2D axisymmetrical model. The pressure field was generated with the bottom of a container oscillating at 33 kHz. Spherical air bubble of resonance size was induced into water near the bottom where it violently collapsed. Compressibility of both phases was taken into account and the interface between air and water was captured using Volume-Of-Fluid approach. Maximal pressures, temperatures and velocities, generated during the collapse, were studied with regard to the initial bubble distance from the bottom. The results were compared for different time step sizes and grid densities where some great differences were found. For validation of the model a separate numerical simulation was run for a bubble collapsing near a rigid wall in a uniform pressure field. The computed bubble shapes were compared to the experimentally observed bubble shapes of Philipp and Lauterborn (1998) and a very good agreement was found. Although the collapse of just one bubble was studied, the results obtained gave good insight into conditions that happen due to cavitation in a near-wall region of ultrasonic cleaning devices.

Key words: Cavitation, Bubble, Collapse, Volume of Fluid, Ultrasound

1. Introduction

Ultrasonic cavitation can be found in many different areas such as chemistry, cleaning, medicine, mixing, biology, ecology etc.[1][2] where favorable effects of collapsing bubbles have been exploited. Bubbles growing in regions of pressure lower than liquid vapor pressure violently collapse in regions of higher pressure, generating extremely high temperatures, pressures and velocities[2][3]. Due to experimental difficulties they can be estimated only in some laboratory cases using special methods such as thermal decomposition[4], high-speed photography[5][6], light emission measurements[7] etc. Because of this, analytical approach to bubble dynamics has been extensively used over the years[2][3]. Its main drawback is that it does not apply to cases where bubble shape is not spherical which in practice happens when a bubble collapses near boundaries[5]. Use of numerical simulations can be especially convenient in such cases, however computer capabilities pose limitations so that only simple cases, e.g. a collapse of a single bubble[8][9][10], can be solved within reasonable time. In this way, a deeper understanding of the ultrasonic cavitation phenomenon can be achieved[11][12], improving the outcome of the processes where it is present.

In our paper a collapse of a single air bubble in water near a solid wall is investigated numerically for a case of an ultrasonic cleaning device. It was described by a 2D axisymmetrical geometry with moving bottom so that the established ultrasonic pressure

field in water was generated in the same way as it is in reality with a piezoelectric transducer mounted on the bottom of the container. Numerical simulations of the collapse of resonance size bubble were done using FLUENT program package[13] for several bubble distances from the wall and Volume-Of-Fluid (VOF) approach[9][14][15] was used to capture the interface between phases, which were both treated as compressible. Maximum values of pressure, velocity and temperature during the collapse were investigated and compared for different time step sizes and grid densities, as these extreme values are the key to cavitation effects.

2. Theoretical formulations

2.1. Spherical bubble in an infinite space

An idealized case of a spherical gas bubble with radius R_0 submerged in an infinite liquid at rest is considered. Other assumptions are that it deforms spherically, that the iquid is Newtonian and noncompressible, and that there is no evaporation, condensation or diffusion of gas over interface. Bubble dynamic is described by Rayleigh-Plesset equation, which in generalized form is[2][3]:

$$\rho\left[R\frac{d^2R}{dt^2}+\frac{3}{2}\left(\frac{dR}{dt}\right)^2\right]+\frac{4\mu}{R}\frac{dR}{dt}=\left(p_{\infty0}-p_v+\frac{2\sigma}{R_0}\right)\left(\frac{R_0}{R}\right)^{3k}-p_\infty+p_v-\frac{2\sigma}{R} \tag{1}$$

For oscillating pressure field, bubble response is also oscillatory. Natural frequency of the bubble can be expressed as[2][16]:

$$\omega_r=\sqrt{\frac{3kp_0}{R^2\rho_L}} \tag{2}$$

If resonance-size bubbles are excited with pressure oscillations of the corresponding resonance frequency, they collapse violently as is the case in ultrasonic cavitation.

2.2. Governing equations for the numerical simulation

2.2.1. Continuity equation

The equation for conservation of mass without any sources can be written as follows

$$\frac{\partial\rho}{\partial t}+\nabla\cdot\left(\rho\vec{v}\right)=0 \tag{3}$$

For 2D axisymmetric geometry, it is given by

$$\frac{\partial\rho}{\partial t}+\frac{\partial}{\partial x}\left(\rho v_x\right)+\frac{\partial}{\partial r}\left(\rho v_r\right)+\frac{\rho v_r}{r}=0 \tag{4}$$

where x is the axial coordinate, r is the radial coordinate, v_x is axial velocity, and v_r is radial velocity.

2.2.2. Momentum conservation equations

Conservation of momentum is described by

$$\frac{\partial}{\partial t}(\rho\vec{v})+\nabla\cdot(\rho\vec{v}\vec{v})=-\nabla p+\nabla\cdot\left(\overline{\overline{\tau}}\right)+\rho\vec{g}+\vec{F} \tag{5}$$

where p is static pressure and $\rho\vec{g}$ and $\vec{F}$ are gravitational body force and the sum of external body forces (e.g., forces that arise from interaction with the dispersed phase), respectively. Stress tensor $\overline{\overline{\tau}}$ is given by

$$\overline{\overline{\tau}}=\mu\left[\left(\nabla\vec{v}+\nabla\vec{v}^T\right)-\frac{2}{3}\nabla\cdot\vec{v}I\right] \tag{6}$$

where μ is molecular viscosity, *I* is the unit tensor, and the second term on the right hand side is the effect of volume dilation.

For 2D axisymmetric geometries, the axial and radial momentum conservation equations are given by

$$\frac{\partial}{\partial t}(\rho v_x) + \frac{1}{r}\frac{\partial}{\partial x}(r\rho v_x v_x) + \frac{1}{r}\frac{\partial}{\partial r}(r\rho v_r v_x) = -\frac{\partial p}{\partial x} + \frac{1}{r}\frac{\partial}{\partial x}\left[r\mu\left(2\frac{\partial v_x}{\partial x} - \frac{2}{3}(\nabla \cdot \vec{v})\right)\right] +$$
$$+ \frac{1}{r}\frac{\partial}{\partial r}\left[r\mu\left(\frac{\partial v_x}{\partial r} + \frac{\partial v_r}{\partial x}\right)\right] + F_x \qquad (7)$$

and

$$\frac{\partial}{\partial t}(\rho v_r) + \frac{1}{r}\frac{\partial}{\partial x}(r\rho v_x v_r) + \frac{1}{r}\frac{\partial}{\partial r}(r\rho v_r v_r) = -\frac{\partial p}{\partial r} + \frac{1}{r}\frac{\partial}{\partial r}\left[r\mu\left(2\frac{\partial v_r}{\partial r} - \frac{2}{3}(\nabla \cdot \vec{v})\right)\right] +$$
$$+ \frac{1}{r}\frac{\partial}{\partial x}\left[r\mu\left(\frac{\partial v_r}{\partial x} + \frac{\partial v_x}{\partial r}\right)\right] - 2\mu\frac{v_r}{r^2} + \frac{2}{3}\frac{\mu}{r}(\nabla \cdot \vec{v}) + F_r \qquad (8)$$

where

$$\nabla \cdot \vec{v} = \frac{\partial v_x}{\partial x} + \frac{\partial v_r}{\partial r} + \frac{v_r}{r}.$$

2.2.3. Energy Conservation Equation

Conservation of energy is in general form described by

$$\frac{\partial}{\partial t}(\rho E) + \nabla \cdot \left(\vec{v}(\rho E + p)\right) = \nabla \cdot \left(k\nabla T - \sum_j h_j J_j + \left(\bar{\bar{\tau}} \cdot \vec{v}\right)\right) + S_h \qquad (9)$$

where

$$E = h - \frac{p}{\rho} + \frac{v^2}{2}.$$

The first three terms on the right-hand side of eq. (9) represent energy transfer because of conduction, species diffusion and viscous dissipation, respectively. The last term represents a volumetric heat source. According to the limitations of the chosen two-phase model (Volume-Of-Fluid model, described in §3.4.), there is no species diffusion and, as there is no condensation or evaporation, the source term is also zero.

3. Numerical method

To solve the time-dependent Navier-Stokes equations for laminar flow a finite-volume method was applied on a 2D grid using FLUENT numerical packet[13]. The SIMPLE algorithm was used for pressure-velocity coupling and implicit time discretization was used. A second-order upwind scheme was used for pressure interpolation. Numerical simulations were computed in double precision with a segregated solver. Convergence criteria were equal for all cases and were 10^{-5} for continuity and momentum equations and 10^{-7} for energy equation. The cases converged on average in $5 - 15$ iterations per time step (more iterations were needed for longer time steps).

3.1. Geometry and grid

A 2D axisymmetrical model shown in Fig. 1 is used to simulate a cylindrical container of an ultrasonic cleaning device. The model was initially meshed with an orthogonal quadrilateral grid, thickening towards the bottom and the axis.
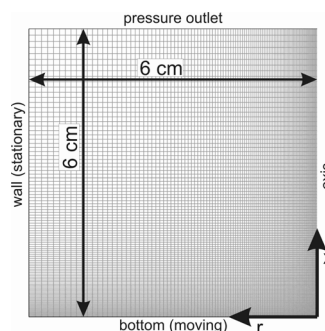
Figure 1: Computational domain

When a bubble was initiated in the domain the grid was refined at the interface so that each cell, for which the gradient of phases was greater than a limit value, was divided in quarters (Fig. 2).
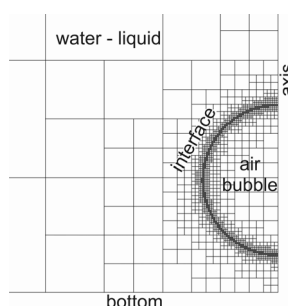

Figure 2: Grid thickening near the interface

Later on during simulation, when bubble shape changed so that the gradient fell lower than the second limit value, cells were merged. Dividing and merging of the cells was performed every second time step during the calculation. Calculations were performed on grids with 5, 6 and 7 levels of grid adaptation. Initial grid characteristics for $\gamma = 1.2$ are presented in Table 1, where γ is the nondimensional initial bubble distance from the wall. It is defined as $\gamma = s_0 / R_0$, where s_0 is the initial distance from the bubble center to the wall and R_0 is the initial bubble radius. For different γ the numbers of nodes and cells presented in Table 1 vary less than 1 %. Dependent on the grid used, time steps used for different cases were from $5 \cdot 10^{-9}$ s to 10^{-7} s.

Table 1: Grids characteristics

	coarse grid	5 levels	6 levels	7 levels
cells	12100	12760	13384	13996
nodes	12321	13077	13787	14568
min cell area* [mm^2]	2.35e-2	2.29e-5	5.73e-6	1.43e-6

*max cell area was the same in all cases and was 1.76 mm^2

3.2. Boundary and operating conditions

For the computational domain presented in Fig. 1 the following boundaries were set: an axis, two walls and a pressure outlet. The side wall was stationary and adiabatic. On the pressure outlet there was a gauge pressure of 100 kPa as the operating pressure was set to zero. Backflow volume fraction for water was set to unity and there was no free surface at the outlet. As buoyancy effects were found to be negligible, in accordance with Tong et al.[17] (1999), gravity was neglected in further calculations.

3.2.1. Moving bottom

The wall representing the bottom of the container was adiabatic and vertically movable (along x axis – see coordinate system position in Fig. 1). With its movements pressure oscillations were generated. Movement of the bottom was described as:

$$x(r,t) = ae^{-br^c} \sin(2\pi f \cdot t) \qquad (10)$$

where f = 33 kHz is the frequency of ultrasound in the container, a = 0.2 µm defines pressure amplitude and the bottom shape is defined by b = -2·10^8 m^{-6} and c = 6. Exponential function was used because assumptions were that there is no vertical movement at the side wall and that the piezoelectric transducer mounted on the opposite side of the bottom would be so stiff that only a part of the bottom not attached to it would deform. Similar amplitude of displacement was used by Bretz et al.[12] (2005). The greatest amplitude of bottom displacement was less than 17 % of the smallest cell length.

3.3. Initial conditions

The initial temperature in the domain was 300 K, the absolute pressure was 100 kPa (in continuation 'pressure' will be used for ease of communication as cavitation always depends on absolute pressure) and there was no velocity. The domain was first filled only with water and a transient pressure field resulting from bottom oscillations was calculated on the coarse grid (Fig. 3).
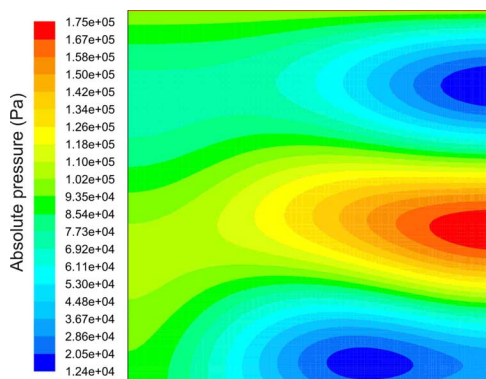

Figure 3: Oscillating pressure field in the domain

When steady oscillations were reached and the pressure in the center of the bottom (r = 0) was minimal, a starting point for two-phase calculation was set. In Fig. 4 courses of pressure (blue) and bottom movement (pink) in the center from the chosen moment on are presented for the primary case with only water in the domain. The displayed timespan is a bit longer than the time of a bubble collapse which is approx. 17 µs as will be presented later.
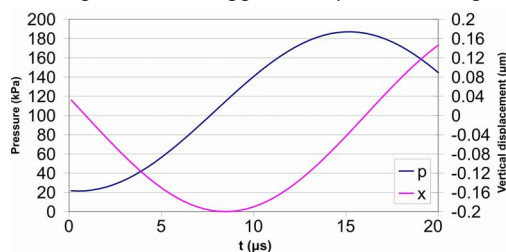

Figure 4: Path of the center of the bottom and the resulting pressure course (case without bubble)

Using the computed pressure field, a spherical air bubble was introduced into water and the grid was refined around the interface (see §3.1, Fig. 2). Resulting from eq. (2), the

bubble of resonance size (regarding the ultrasound of 33 kHz) with radius of 100 μm was introduced in the axis close to the center of the bottom, because in case of ultrasonic cavitation only bubbles of   resonance size collapse violently[1][2][18].

For different cases considered, a bubble was placed from the wall at γ ranging from 1.01 to 1.5 as the cavitation effects are very strong in this region[5]. The initial bubble shape was assumed spherical.

3.4. Volume-Of-Fluid model

The Volume-Of-Fluid (VOF) two-phase model[19] is used to describe the behavior of an air bubble (primary phase) in liquid water (secondary phase), assuming that the phases are not interpenetrating. Surface tracking between phases is done by solving a continuity equation for the volume fraction of the second phase:

$$\frac{\partial}{\partial t}\left(\alpha_2 \rho_2\right) + \nabla \cdot \left(\alpha_2 \rho_2 \vec{v}_2\right) = 0 \qquad (11)$$

The right side of eq. (11) is zero as there are no sources (evaporation or condensation) because of the limitations of the model which does not enable them. Equation (11) is solved using an explicit time-marching scheme. The volume fraction for the first phase is computed from the constraint that the volume fractions of both phases sum to unity. Knowing the volume fraction α of the phase in the computational cell, the fields for all variables and properties are shared by the phases and represent volume-averaged value at each location. For example, density in a cell is defined as

$$\rho = \alpha_2 \rho_2 + (1 - \alpha_2)\rho_1 \qquad (12)$$

In this manner a single momentum and a single energy equation are solved.

Both phases are considered compressible: air properties are defined by the ideal gas law while water density depends on pressure in the following manner:

$$\rho = \frac{\rho_0}{1 - \dfrac{\Delta p}{K}} \qquad (13)$$

K is water bulk modulus and Δp is pressure difference with regard to the outside pressure (1 bar).

3.4.1. Geometric reconstruction scheme

For the interpolation near the surface a geometric reconstruction scheme[20] was used to calculate face fluxes. The geometric reconstruction scheme represents the interface between fluids using a piecewise-linear approach[21], assuming that the interface has a linear slope within each cell, and uses this linear shape for calculation of the advection of fluid through the cell faces. First, the position of the linear interface relative to the center of each partially-filled cell is calculated, based on the volume fraction and its derivatives in the cell. Secondly, the advecting amount of fluid through each face is calculated using the computed linear interface representation and information about the normal and tangential velocity distribution on the face. Finally, the volume fraction in each cell is calculated using the balance of fluxes from the previous step.

3.4.2. Surface tension

The effect of surface tension[22] is included in the VOF model. It is modeled using the continuum surface force (CSF) model[23], where surface tension is included as a source term in the momentum equation. It has a form of a volume force in which the force at the surface is expressed as

$$F_{vol} = \sigma_{ij} \frac{\rho \chi_i \nabla \alpha_i}{\frac{1}{2}(\rho_i + \rho_j)} \tag{14}$$

Curvature of the surface χ is defined as the divergence of the unit normal $\chi = \nabla \cdot \frac{n}{|n|}$, where the surface normal is $n = \nabla \alpha$, $\nabla \alpha_i = -\nabla \alpha_j$ and $\chi_i = -\chi_j$. In the performed numerical simulations a surface tension coefficient $\sigma = 0.072$ N/m was used.

4. Results and discussion

4.1. Comparison with the experiment

Bubble contours from the numerical simulation were compared to the experimentally obtained photographs of a single bubble collapse from Philipp and Lauterborn[5] (1998) for the same initial – maximum radius (R = 1.45 mm), stand-off distance from the wall ($\gamma = 1.2$) and operating pressure. They are displayed in Fig. 5 using the same time step between the frames.
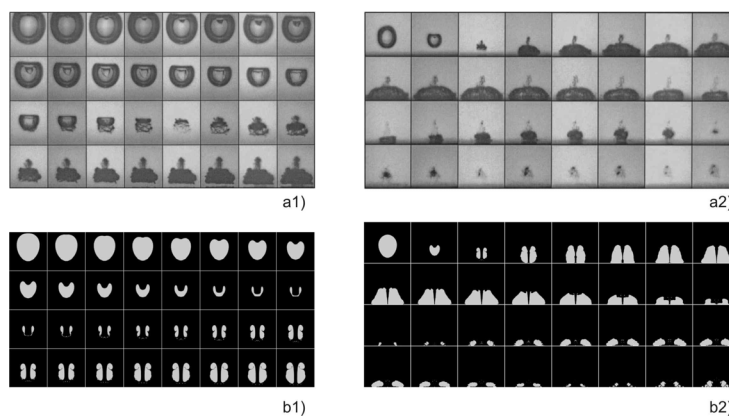

Figure 5: Cavitation bubble dynamics a) photographs from Philipp and Lauterborn[5] reproduced with permission of the second author, b) contour diagrams of phases from numerical simulation; time between frames 1) 1 μs, 2) 17.7 μs

The main difference between the calculated bubble shapes and the experimental observations is in a counterjet presence. As it is not the part of the original bubble but appears during the collapse by evaporation[24], it is clear that the two-phase model not taking into account phase changes is missing it. It can be also observed that towards the end of the series the differences in bubble shape and position are more pronounced. For the numerical part, this is probably another effect of not considering the phase changes, while on the other hand the experimental results carry some uncertainty about geometric data (R, γ) and the possible effect of graphical perspective. The last might be the reason for the greater bubble distance from the wall in the case of the experiment (if the optical axis is not coinciding with the wall).

However, regarding the same frame size and the same time step between numerical and experimental frames, numerical results follow the bubble shape evolution in experimental photographs. Considering also a comparison from Mousavi and Ahmadi[9] between the similar numerical model and the experimental results (from Ishida et al.[25]), it is believed that the presented numerical model can be applied to simulate a cavitation bubble collapse.

4.2. Numerical simulation of the nonspherical collapse

Several different cases of bubble collapse were considered, differing on the distance

from the wall, grid density (expressed in terms of levels of refinement) and time step. Results for maximal values in the domain for pressure, temperature and velocity and maximal pressure in the center of the bottom are presented on the diagrams below for a time period corresponding to the final stage of the bubble collapse. On each diagram, bubble contours at corresponding moments in time are displayed for one of the presented cases.

Maximal temperatures are ranging from approx. 760 K to 850 K and are reached when the bubble is the most compressed (Fig. 6). As γ increases, wall effect is smaller (spherical shape of the bubble is retained farther) and so the bubble is more compressed and collapses faster, meaning also a smaller heat transfer from air to water. General trend can be observed of the maximal temperatures rising with the increasing γ, although for some cases peak maximal temperatures do not follow the exact order. This is probably related to the grid dividing and merging, where for more deformed bubbles the bubble interior consists of smaller cells, whereas for more spherical bubbles the center of the bubble is farther from the boundary (where the cells are the smallest) so in the center there might be larger cells (see Fig. 2). So due to the spatial averaging over larger cells the maximal temperatures could appear smaller.
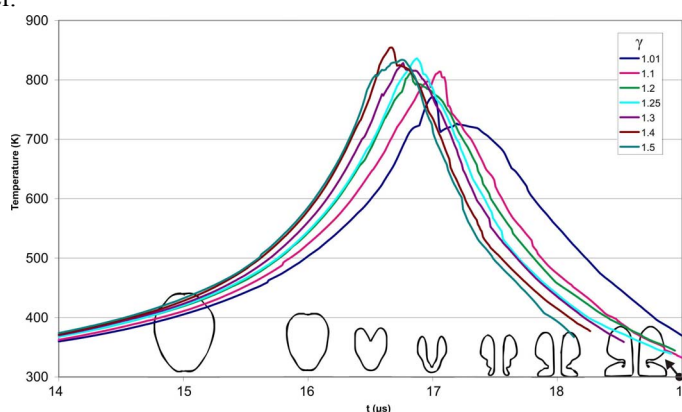

Figure 6: Maximal temperature for different bubble distances from the bottom; $\Delta t = 10^{-8}$ s, 7 levels of grid refinement, bubble contours for pink curve ($\gamma = 1.1$)

Dependence of the maximal pressure in the center of the bottom on γ is even greater (Fig. 7). When γ changes from 1.01 to 1.2, the maximal pressure decreases approx. to one fourth. The reason is that a peak value of the maximal pressure happens when a microjet strikes the surface, while for $\gamma < 1.2$ the bubble is so close to the bottom that the water between them is almost completely removed in the first part of the collapse, so that the generated microjet goes through the air and hits the bottom directly (compare the contours in Figs. 7 and 9).
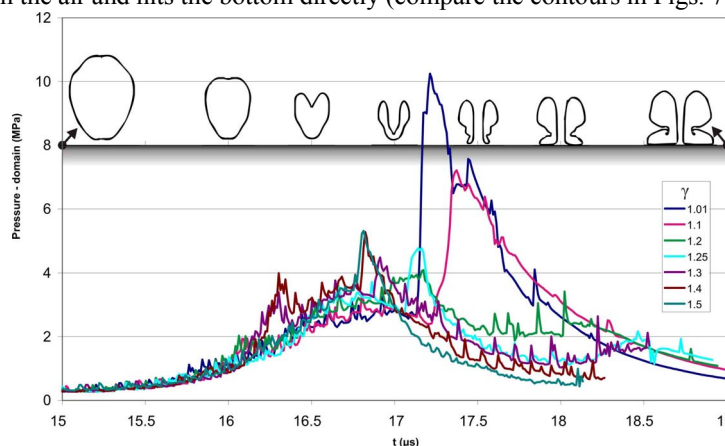

Figure 7: Maximal pressure for different bubble distances from the bottom; $\Delta t = 10^{-8}$ s, 7 levels of grid refinement, bubble contours for pink curve ($\gamma = 1.1$)

With an increasing γ, the amount of water between the bubble and the wall is thicker, so the microjet velocity decreases when it hits the bottom, thus reducing the pressure load on the bottom. The impact of a liquid jet on a solid surface generates a water hammer pressure, after this, the pressure decreases to the stagnation pressure.[5]

However, from the compressed bubble a shock wave is emitted which is recognized as a main mechanism for erosion effects [5] and might be treated as such also for cavitation cleaning. But if the results of the maximal pressure in the domain are compared to the maximal pressure in the center of the bottom (Fig. 8 left and right), it can be seen that the shock wave is not expressed as heavily as expected[5], because peak values result in both cases from the jet impact. The reason why the shock wave is not sufficiently captured is probably in the grid formation (as mentioned before about the temperature - whereas the grid is fine enough to capture well the bubble shape it degrades soon with the increasing distance from the interface). Effect of grid on the results is further presented in Fig. 8. Finer grid can better describe large gradients on the interface so the phenomena at the collapse are more expressed (higher pressure peaks etc.). Convergence of results with grid thickening can also be observed, indicating that even finer grids may be used.
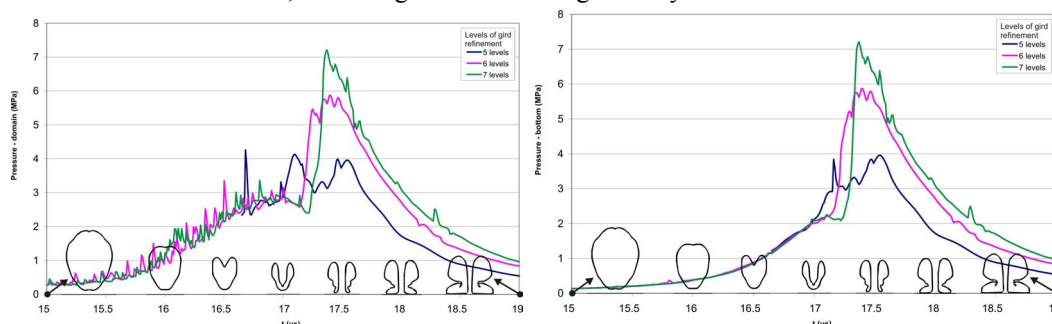

Figure 8: Maximal pressure in the domain (left) and in the center of the bottom (right) for different grid densities; $\Delta t = 10^{-8}$ s, $\gamma = 1.1$, bubble contours for green curves (7 levels of grid refinement)

The effect of the time step size on the results is presented for maximal velocity and maximal temperature in the domain in Figs. 9 and 10. It is smaller than the effect of grid density as the results are alike for all cases. However, for the courses of the maximal velocities presented in Fig. 9, some major differences can be observed at the beginning and at the end. Therefore the explanation of the maximal velocity course is needed.

At the beginning (e.g. 15 μs), bubble was collapsing slowly, allowing enough of time (steps) for remeshing so that its interface was always captured by the best available grid. Thus so far all courses are going likewise.

Further on (from e.g. 15.5 μs), the part of the bubble far from the wall was heavily accelerated towards the wall and the maximal velocities were resulting from that part of the interface, which shape was changing from concave to convex. Accelerations of the interface were so great that the grid was not able to adjust so fast to the changes of its position. So the oscillations in that part are resulting from the grid adjustments which were done every second time step. Oscillations may be reduced by remeshing on every time step and by using shorter time steps, although it must be stressed that convergence criteria were reached in all cases.

From approx. 16.5 to 18 μs, maximal velocities were that of a microjet. Once the grid was already dense in that part, the velocity course is smooth. As expected, the velocity was decreasing when the bubble was expanding.

At the last part of the course (e.g. from 18 μs on), two phenomena occurred. One is that the grid in some parts of the bubble was already getting coarse and the other is that the maximal velocity occurred inside of the bubble, where the expanding air started to swirl, in that way reaching much higher velocities than the interface. The result are high variations in

the maximal velocity course, which also reaches previously unexpectedly high values. The effect of the numerical error was found minute as a very high repeatability of the results was obtained.
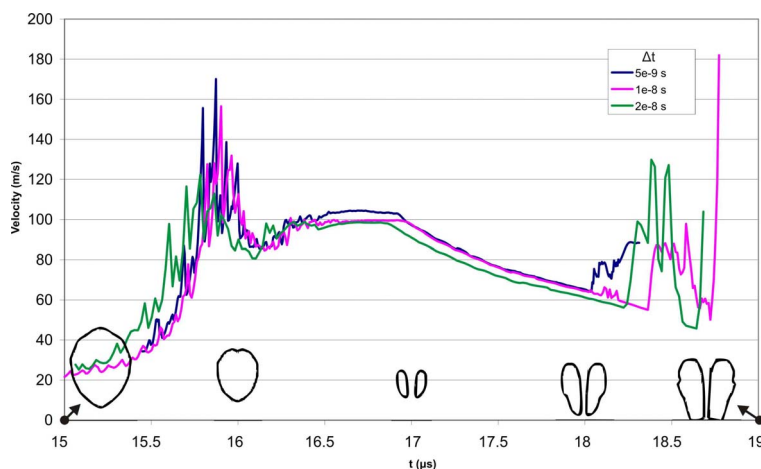

Figure 9: Maximal velocity for different time steps; $\gamma = 1.2$, 6 levels of grid refinement, bubble contours for green curve ($\Delta t = 2 \cdot 10^{-8}$ s)

Comparing temperature courses in Fig. 10, time step size has little effect. Also the maximal temperatures of approx. 780 K are reached in all three cases.
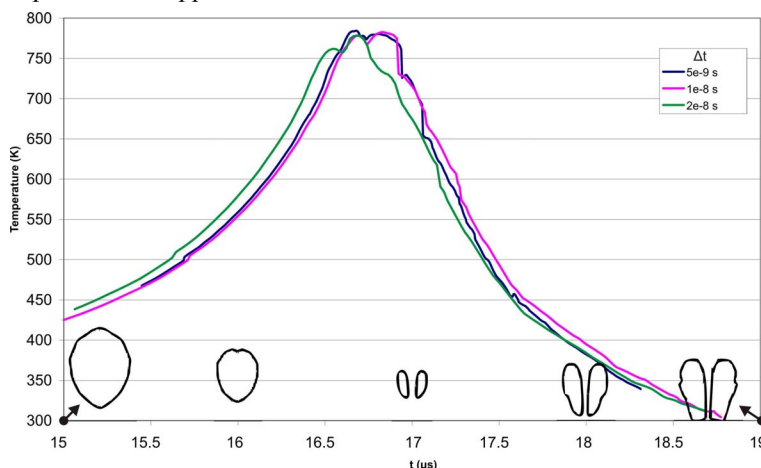

Figure 10: Maximal temperature for different time steps; $\gamma = 1.2$, 6 levels of grid refinement, bubble contours for green curve ($\Delta t = 2 \cdot 10^{-8}$ s)

5. Conclusion

Numerical simulations of a bubble collapsing in an ultrasonic field near a solid boundary were performed with FLUENT program package using VOF approach to capture the interface between the air bubble and liquid water compendium. Different bubble distances from the moving solid bottom were considered and the effects of grid density and time step size were observed at the maximal pressure, temperature and velocity values. For the initial and boundary conditions, resembling the ones in an ultrasonic cleaning device, the maximal temperatures and pressures were approx. 800 K and 2 – 10 MPa. The maximal reported velocities were up to 170 m/s while microjet velocities were around 100 m/s. The conditions at the collapse were mostly affected by the bubble shape during it, which was dependent on the bubble distance from the bottom. The results were greatly influenced by the grid density while the time step size had less influence as long as the same convergence criteria were fulfilled.

Nomenclature

Roman letters

a	coefficient (eq. 13, m)
b	coefficient (eq. 13, m^{-6})
c	coefficient (eq. 13, -)
E	energy (J)
f	frequency (Hz)
F	force (N)
g	gravitational acceleration ($m\,s^{-2}$)
h	specific enthalpy ($J\,kg^{-1}$)
I	unit tensor (-)
J	diffusion flux ($kg\,m^{-2}\,s^{-1}$)
k	polytrophic coefficient (-)
K	bulk modulus (Pa)
m	mass (kg)
n	surface normal (-)
p	pressure (Pa)
r	radial coordinate (m)
R	radius (m)
s	distance from the bubble center to the wall (-)
S	source term (units vary)
t	time (s)
v	velocity ($m\,s^{-1}$)
x	x coordinate (m)

Greek letters

α	volume fraction (-)
γ	nondimensional bubble distance from the wall (-)
κ	isentropic coefficient (-)
μ	dynamic viscosity ($kg\,m^{-1}\,s^{-1}$)
ρ	density ($kg\,m^{-3}$)
σ	surface tension ($N\,m^{-1}$)
τ	stress tensor (Pa)
χ	curvature of the surface (-)
ω	angular frequency (s^{-1})

Subscripts

0	initial
1	of the first phase
2	of the second phase
∞	far away
i	component
j	component
L	liquid
max	maximal
min	minimal
r	resonance, in radial direction
v	vapor
x	in x direction

References

(1) Mason T. J., Lorimer J. P.: Applied Sonochemistry, Wiley-VCH, 2002

(2) Young F. R.: Cavitation, McGraw-Hill, 1989

(3) Brennen C. E.: Cavitation and Bubble Dynamics, Oxford University Press, 1995

(4) Rae J. et al.: Estimation of ultrasound induced cavitation bubble temperatures in aqueous solutions, *Ultrasonics Sonochemistry*, Vol. 12 (2005) pp. 325-329

(5) Philipp A., Lauterborn W.: Cavitation erosion by single laser-produced bubbles, *J. Fluid Mech.*, Vol. 361 (1998) pp. 75-116

(6) Shima A.: Studies on bubble dynamics, *Shock Waves*, Vol. 7 (1997) pp. 33-42

(7) Chakravarty A., Walton A. J.: Light emission from collapsing superheated steam bubbles in water, *J. of Luminiscence*, Vol. 92 (2001) pp. 27-33

(8) Tsiglifis K., Pelekasis N. A.: Numerical simulations of the aspherical collapse of laser and acoustically generated bubbles, *Ultrasonics Sonochemistry*, Vol. 14 (2007) pp. 456-469

(9) Mousavi R. B. T., Ahmadi G.: Intensification of the Near Wall Collapsing Bubble Induced Jet Using an Opposite Secondary Wall, *J. of Fluid Science and Technology*, Vol. 3 (1) (2008) pp. 207-218

(10) Nagrath S. et al.: Hydrodynamic simulation of air bubble implosion using a level set approach, *J. of Computational Physics*, Vol. 215 (2006) pp. 98-132

(11) Servant G. et al.: Numerical simulation of cavitation bubble dynamics induced by ultrasound waves in a high frequency reactor, *Ultrasonics Sonochemistry*, Vol. 7 (2000) pp. 217-227

(12) Bretz N. et al.: Numerical simulation of ultrasonic waves in cavitating fluids with special consideration of ultrasonic cleaning, IEEE Ultrasonics Symposium (2005) pp. 703-706

(13) FLUENT 6.2 Documentation, Fluent Inc., 2005

(14) van Sint Annaland M., Deen N. G., Kuipers J. A. M.: Numerical simulation of gas bubbles behaviour using a three-dimensional volume of fluid method, *Chemical Engineering Science*, Vol. 60 (2005) pp. 2999-3011

(15) Crespo A., Jiménez-Fernández J.: Bubble oscillation and inertial cavitation in viscoelastic fluids, *Ultrasonics*, Vol. 43 (2005) pp. 643-651

(16) Devaud M. et al.: The Minnaert bubble: an acoustic approach, *Eur. J. Phys.,* Vol. 29 (2008) pp. 1263-1285

(17) Tong R. P. et al.: The role of 'splashing' in the collapse of a laser-generated cavity near a rigid boundary, *J. Fluid Mechanics*, Vol. 380 (1999) pp. 339-361

(18) Ashokkumar M. et al.: Bubbles in an acoustic field: An overview, *Ultrasonics Sonochemistry*, Vol. 14 (2007) pp. 470-475

(19) Hirt C. W., Nichols B. D.: Volume of Fluid (VOF) Method for the Dynamics of Free Boundaries, *J. Comput. Phys.*, Vol. 39 (1981) pp. 201-225

(20) Youngs D. L.: Time-Dependent Multi-Material Flow with Large Fluid Distortion, Numerical Methods for Fluid Dynamics, Academic Press, 1982

(21) Sou A., Hayashi K., Nakajima T.: Evaluation of volume tracking algorithms for gas-liquid two-phase flows, Proceedings of ASME FEDSM'03, 2003

(22) Gerlach D. et al.: Comparison of volume-of-fluid methods for surface tension-dominant two-phase flows, *Int. J. of Heat and Mass Transfer*, Vol. 49 (2006) pp. 740-754

(23) Brackbill J. U., Kothe D. B., Zemach C.: A Continuum Method for Modeling Surface Tension, *J. Comput. Phys.*, Vol. 100 (1992) pp. 335-354

(24) Lindau O., Lauterborn W.: Investigation of the counterjet developed in a cavitation bubble that collapses near a rigid boundary, *Proc. of CAV2001 Conf.*, 2001

(25) Ishida H. et al.: Cavitation bubble behavior near solid boundaries, *Proc. of CAV2001 Conf.*, 2001